





## 1 1 Introduction

2 Arctic mixed-phase stratocumulus clouds (AMPS) play a unique role in climate by producing  
3 a net warming at the Earth's surface over the annual cycle. This warming is due to the limited  
4 amount of incoming solar radiation at high latitudes, causing downward longwave radiative  
5 effects to dominate surface cloud forcing in the Arctic. AMPS are characterized by a liquid  
6 cloud layer with ice crystals that precipitate from cloud base even at temperatures well below  
7 freezing (Hobbs and Rangno, 1998; Intrieri et al., 2002; McFarquhar et al., 2007). The  
8 magnitude of the cloud-forced surface warming is primarily a function of the liquid water  
9 content of the AMPS and the properties of the cloud droplets (Curry and Ebert 1992; Curry et  
10 al. 1993; Zhang et al. 1996) However, different from warm clouds, the magnitude and  
11 properties of cloud liquid in mixed-phase clouds are closely connected to the formation of  
12 cloud ice, which limits the availability of water vapor for droplet formation and growth (the  
13 Wegener-Bergeron-Findeisen (WBF) mechanism, Wegener, 1911; Bergeron, 1935; Findeisen,  
14 1938) and acts as a sink for water vapor through the growth and sedimentation of frozen  
15 precipitation.

16 Cloud ice in AMPS must form through heterogeneous nucleation, since temperatures are too  
17 warm for homogenous ice nucleation (approximately  $> 36$  °C). Heterogeneous ice nucleation  
18 can occur by a number of modes: either in the presence of super-cooled droplets, when an  
19 aerosol comes into contact with a droplet (contact freezing), is immersed in a droplet followed  
20 by freezing (immersion freezing), or in the absence of droplets through vapor deposition on  
21 aerosol (deposition freezing) or liquid forming on aerosol (condensation freezing) (Pruppacher  
22 and Klett, 1997). The efficiency of any of these modes in a given environmental state is a  
23 function of aerosol properties, which determine whether an aerosol can serve as an ice  
24 nucleating particle (INP), cloud condensation nucleus (CCN), or both. Based on measurements  
25 from in situ instrumentation and the reduced concentration of ice crystals relative to liquid  
26 droplets (Murray et al., 2012), it is believed that only a small fraction of aerosols can serve as  
27 INPs. For example, in the Indirect and Semi- Direct Aerosol Campaign (ISDAC) (McFarquhar  
28 et al., 2011) that took place off the coast of Utqiagvik, (Barrow) Alaska in the spring of 2008,  
29 the number of INPs available were observed to be four orders of magnitude smaller than the



1 number of aerosols serving as CCN. However, it is important to note that only a few INPs are  
2 needed to glaciate a cloud (see discussion in DeMott et al. 2010).

3 The impact of CCN variability on warm cloud structure has been the subject of numerous  
4 papers. For a fixed liquid water path (LWP), an increase in CCN in warm clouds will increase  
5 the number of droplets and reduce the droplet size. This causes an increase in cloud albedo (the  
6 Twomey effect; Twomey, 1977) and potentially suppresses precipitation (the Albrecht effect;  
7 Albrecht 1989). Suppressing precipitation can increase cloud thickness/coverage and cloud-  
8 driven turbulence, which increases the entrainment of dry air at cloud top, thereby thinning the  
9 cloud (Pincus and Baker, 1994; Stevens et al., 1998). This thinning of the cloud as a response  
10 to an increase in aerosols is an example of a buffering feedback that limits the impact of a CCN  
11 perturbation on the cloud structure (Stevens and Feingold, 2009). For LWPs greater than  
12 approximately  $50 \text{ gm}^{-2}$ , AMPS emit as blackbodies (Shupe and Intrieri, 2004) and an increase  
13 in CCN has minimal impact on longwave emissivity (Morrison et al., 2008). However, smaller  
14 droplets can also reduce the ice water path (IWP) through a reduction in collision-coalescence  
15 and riming of snow by droplets (Morrison et al., 2008), as well as, make ice nucleation less  
16 efficient (Lance et al. 2011). These are only a few examples of buffering feedbacks that exist  
17 in mixed-phase clouds.

18 An increase in INPs in AMPS is known to produce a “glaciation effect”, i.e., a rapid depletion  
19 of cloud liquid, in part due to the WBF mechanism and the acceleration of frozen precipitation  
20 (Murray et al., 2012). However, the efficacy of this effect is dependent upon the chemical  
21 composition of the INPs. In cases where INPs are transported over long distances and coated  
22 in sulfate or organic materials, an increased concentration of INPs may actually be linked to a  
23 “deactivation effect”. This is because coated particles generally freeze at colder temperatures  
24 (Cziczo et al., 2009; Sullivan et al., 2010; Girard and Sokhandan, 2014), changing the number,  
25 size and fall speeds of nucleated ice crystals and increasing cloud lifetime. The deactivation  
26 effect can cause a significant increase in surface warming, since a decrease in droplet size in  
27 optically thin clouds for constant LWP can produce a significant increase in cloud longwave  
28 emissivity (Garrett and Zhao, 2006).



1 Given the uncertainty in measurements of INPs (DeMott, 2015; Garimella et al., 2017), it has  
2 been challenging to study the manifestation of aerosol-cloud interactions in mixed-phase cloud  
3 conditions. This study investigates these interactions and their dependence on aerosol  
4 partitioning in idealized large-eddy simulations (LES) of an AMPS observed at Oliktok Point,  
5 Alaska 5-17Z 17 April 2015. In order to isolate the impact of these interactions on longwave  
6 cloud forcing, shortwave radiation is neglected in the simulations. The microphysics used in  
7 Solomon et al. (2015) have been modified to include prognostic CCN in addition to prognostic  
8 INPs. This allows for a more realistic representation of aerosols advected over the Oliktok  
9 Point site. In order to identify aerosol indirect effects in these simulations, aerosol chemistry  
10 is specified and, due to the in-cloud temperatures for this case, all cloud ice forms through  
11 immersion freezing. The focus on immersion freezing is supported by studies demonstrating  
12 that liquid droplets typically form prior to ice formation in mixed-phase cloud environments  
13 (e.g. de Boer et al., 2011; Westbrook and Illingworth, 2012).

14 This study is focused on the research questions:

- 15 1) What is the relative impact of CCN versus INP perturbations on the phase partitioning  
16 between cloud liquid and cloud ice in AMPS? Specifically, what is the impact on cloud  
17 dynamics?
- 18 2) Are there buffering feedbacks in AMPS that limit the impact of CCN/INP  
19 perturbations?

## 20 **2 Case Description**

21 Simulations are set up to recreate conditions observed by the US Department of Energy (DOE)  
22 Atmospheric Radiation Measurement (ARM) program third mobile facility (AMF-3) at  
23 Oliktok Point, Alaska on and around 17 April 2015 (Figure 1). During this time period, Oliktok  
24 Point was situated in a relatively quiet regime synoptically, with surface high pressure to the  
25 northwest over the Chukchi Sea, and a weak area of low pressure over central Alaska. This  
26 resulted in steadily increasing surface air pressure from around 1008 hPa at 00Z on 16 April  
27 to around 1021 hPa at 00Z on 18 April and relatively light ( $2\text{-}5\text{ m s}^{-1}$ ) near-surface winds ( $U_{10m}$ )  
28 from the east-northeast over this entire two-day window (Figures 1f,g). Near-surface air  
29 temperatures ( $T_{2m}$ ) varied dramatically (Figure 1e), depending on time of day and cloud cover,



1 with the coldest temperatures around 250 K during late evening and early morning clear  
2 periods on 16 April, and the warmest temperatures being around 258 K during cloudy periods  
3 during local night time on 17 April. Near-surface relative humidity ( $RH_{2m}$ ) showed a weak  
4 diurnal signature, ranging from around 80% during local daytime hours and 86-88% during  
5 nighttime hours.

6 Radiosonde launches conducted at approximately 2330 UTC on 15 April, 1730 UTC and 2330  
7 UTC on 16 April, and 1830 UTC and 2330 UTC on 17 April reveal the evolution of the lower  
8 troposphere at Oliktok Point (Figure 1h). The 2330 UTC sounding from 15 April reveals a  
9 well-mixed surface layer extending up to around 200 m, a stable layer from 200-700 m and  
10 then an elevated layer that is generally well mixed from 700-2000 m. By 1730 UTC a strong  
11 inversion formed from 30-300 m above the surface where there is a residual mixed layer from  
12 the previous night's cloud cover between 300-600 m. Above this layer, there is a weakly stable  
13 layer from 600 m to around 1000 m. A similar vertical structure persists through the rest of  
14 the sampling period, with the strength of the near-surface inversion and depth of the overlying  
15 mixed layer evolving with time, and general warm-air advection occurring above 1000 m.  
16 With the exception of a very dry layer between 200-350 m in the 2330 UTC sounding on 17  
17 April, and a saturated layer around 200 m in the 1730 UTC sounding on 16 April, the lower  
18 atmosphere (0-700 m) features relative humidity between 70-90%. Above this, RH values  
19 feature variability between 30-60%, with the height at which this drop off occurs increasing  
20 with time. The last two soundings are substantially drier between 1200-2000 m, with RH  
21 values around 20%.

22 On both 16 and 17 April, low-level mixed-phase stratus cloud layers were observed to develop  
23 during local night time (~0600-1800 UTC). Surface radiation measurements (Figures 1c,d)  
24 clearly demonstrate the presence of these clouds, with the net longwave radiation ( $LW_{NET}$ )  
25 increasing to around  $0 \text{ W m}^{-2}$  as a result of increased downwelling longwave ( $LW_{DOWN}$ ) during  
26 cloudy periods. An increase in downwelling shortwave radiation may be playing a role in the  
27 dissipation of the cloud layer. The presence of cloud is also detected by active remote sensors  
28 (Figure 1a), with ceilometer cloud base (black dots) and Ka-band cloud radar reflectivity  
29 (colored shading) measurements clearly showing the nighttime appearance of liquid-  
30 containing cloud layers between 450 and 700 m (on 16 April) and 800 and 1000 m (on 17



1 April) above the surface, with the cloud on 17 April starting and ending with lower cloud bases  
2 and tops. Both radar and surface precipitation gauges indicated weak snowfall associated with  
3 these clouds and shortwave irradiance measurements reveal that the surface was snow covered  
4 during this time, with surface albedo around 80%.

### 5 **3 Model Description**

6 Simulations are completed using the large eddy simulation mode of the Advanced Research  
7 WRF model (WRFLES) version 3.3.1 (Yamaguchi and Feingold, 2012) with the RRTMG  
8 longwave radiation parameterization (Mlawer et al., 1997) and the Morrison two-moment  
9 microphysical scheme (Morrison et al., 2009). Collision-coalescence was found to be  
10 important in CCN perturbation studies during the Fall 2004 Mixed-Phase Arctic Cloud  
11 Experiment (M-PACE; Morrison et al, 2008), however tests with and without riming and  
12 collision-coalescence indicated that these processes are not significant for this case and have  
13 been neglected in the simulations. Shortwave radiation is neglected given the nighttime  
14 occurrence of these clouds and to be able to focus on longwave indirect aerosol effects. Surface  
15 fluxes are calculated using the modified MM5 similarity scheme, which calculates surface  
16 exchange coefficients for heat, moisture, and momentum following Webb (1970) and uses  
17 Monin–Obukhov with Carlson–Boland viscous sublayer and standard similarity functions  
18 following Paulson (1970) and Dyer and Hicks (1970). The land surface is simulated with the  
19 unified Noah land-surface model (Tewari et al., 2004). Initial surface pressure is 1020 hPa.  
20 The initial surface temperature is 255 K.

21 All simulations are run on a domain of  $3.6 \times 3.6 \times 1.4$  km with a horizontal grid spacing of 50  
22 m and vertical spacing of 10 m. The domain has  $72(x) \times 72(y) \times 140(z)$  grid points and is  
23 periodic in both the x and y directions. The top of the domain is at 1.4 km. The model time  
24 step is 0.5 seconds.

#### 25 ***a. Initial atmospheric profiles***

26 Initial profiles of temperature, moisture and horizontal wind components are based on  
27 radiosonde measurements taken at Oliktok Point at 23:30Z 16 April 2015 (Figure 1h).  
28 Soundings are not available during the cloudy period (5-18Z), seen in the KAZR reflectivity



1 (Figure 1a). Therefore, the model is initialized with a cloud free sounding and the cloud forms  
2 in response to the radiative cooling, rather than starting the stimulation with a “cloudy” profile  
3 and requiring the cloud ice and liquid to adjust to the initial state. The potential temperature  
4 and water vapor mixing ratio from the radiosonde and the initial profiles used in the simulations  
5 are shown in Figure 2. Initial water vapor is increased in the region where cloud liquid water  
6 was observed after 5Z in order to produce cloud liquid water at the start of the integration.  
7 Initial temperature and subgrid TKE are perturbed below the top of the mixed layer with  
8 pseudo-random fluctuations with amplitude of 0.1 K and  $0.1 \text{ m}^2 \text{ s}^{-2}$ , respectively.

### 9 ***b. Large-scale forcing***

10 Large-scale subsidence is specified by integrating the prescribed horizontal wind divergence  
11 from the surface upward. Divergence is assumed to be equal to  $1.8 \times 10^{-6} \text{ s}^{-1}$  below the  
12 inversion and zero above, following the Solomon et al. (2015) study. This gives a linear  
13 increase in large-scale subsidence from zero at the surface to  $1.5 \text{ mm s}^{-1}$  at the base of the  
14 initial inversion ( $z=805 \text{ m}$ ), above which the large-scale vertical wind is constant. Large-scale  
15 subsidence is accounted for via a source term for any prognostic variable other than wind  
16 components.

17 Temperature and moisture profiles are nudged to the initial profiles in the top 100 meters of  
18 the domain with a time scale of 1 hour. Horizontal winds are nudged to the initial profiles at  
19 and below the initial inversion base with a timescale of 2 hours. Nudging of the horizontal  
20 wind components, temperature and moisture profiles is performed by adding a source term to  
21 the prognostic equations for potential temperature, water vapor, and horizontal wind  
22 components.

### 23 ***c. Droplet number concentration and CCN properties***

24 Because CCN measurements were not available from Oliktok Point during this time, initial  
25 CCN size distributions at every gridpoint are based on springtime measurements taken during  
26 the ISDAC campaign (Earle et al. 2011). The accumulation mode observed during ISDAC had  
27 a concentration of less than  $200 \text{ cm}^{-3}$  ( $165 \text{ cm}^{-3}$  used in this study), a modal diameter of 0.2  
28 microns, and a geometric standard deviation of 1.4. Sensitivity studies vary initial CCN



1 concentration with an arbitrary multiplication factor  $C$  (referred to as the CCN factor). CCN  
2 mean concentration is then treated as a prognostic variable. A prognostic equation for CCN  
3 number concentration has been added to WRFLES,

$$4 \quad \frac{\partial CCN}{\partial t} + ADV + DIFF = \frac{\delta CCN}{\delta t} \Big|_{condensation} + \frac{\delta CCN}{\delta t} \Big|_{evaporation} \quad (1)$$

5 where ADV represents advection and DIFF represents turbulent diffusion. Condensation is a  
6 sink of CCN and evaporation is a source of CCN. Evaporation (condensation) of one droplet  
7 produces (removes) one CCN.

8 Cloud droplets are activated using resolved and subgrid vertical motion (Morrison and Pinto,  
9 2005) and a log-normal aerosol size distribution (assumed to be ammonium bisulfate and 30%  
10 insoluble by volume) to derive cloud condensation nuclei spectra following Abdul-Razzak and  
11 Ghan (2000). As noted in Solomon et al. (2015), because the aerosol number size distribution  
12 peaks at a relatively large diameter of 0.2 microns, the majority of CCN activate into droplets  
13 at low supersaturation (at or below  $SS_w = 0.15\%$ ) for a reasonable range of aerosol composition  
14 assumptions. Since such supersaturations can be generated even by slow updrafts, the  
15 sensitivity of droplet number concentration to aerosol composition is expected to be weak. We  
16 therefore only include simulations that test the sensitivity to mean CCN concentrations.

#### 17 ***d. Ice nucleation***

18 Following Solomon et al. (2015), a prognostic equation for INP number concentration ( $N_{INP}$ )  
19 has been added to WRFLES,

$$20 \quad \frac{\partial N_{INP}}{\partial t} + ADV + DIFF = \frac{\delta N_{INP}}{\delta t} \Big|_{activation} + \frac{\delta N_{INP}}{\delta t} \Big|_{sublimation} \quad (2)$$

21 where ADV represents advection and DIFF represents turbulent diffusion. Activation is also  
22 referred to as ice nucleation and sublimation represents a source of INP, supporting the  
23 recycling of these particles.



1 Eight prognostic equations are integrated for  $N_{INP}$  in equally spaced temperature intervals with  
2 nucleation thresholds spanning the range of the in-cloud temperatures (-20.15°C to -14.55°C).  
3 Therefore, additional INP become available for activation with decreasing temperature and as  
4 the cloud layer cools. INP number concentrations are initially specified at 1.3 L<sup>-1</sup> in each bin  
5 to produce IWP close to observations for this case. Sensitivity studies vary initial INP  
6 concentration with an arbitrary multiplication factor  $F$  (referred to as the INP factor).

7 It is assumed that 50% of the INP available in a bin nucleate if the in-situ temperature is below  
8 the threshold temperature and the local conditions exceed water saturation. Therefore, initial  
9  $N_{INP}$  are a function of the nucleation threshold temperatures and are independent of the in-situ  
10 temperature. The in-situ temperature in regions of water saturation determines how many INP  
11 are activated. Due to the pristine dendritic nature of the observed crystals and the limited  
12 number of INP, ice shattering and aggregation are neglected in the simulations and sublimation  
13 returns one INP per sublimated crystal.

14  $N_{INP}$  (in units of L<sup>-1</sup>) integrated over the domain in each temperature bin  $k$  at time  $t$  is equal  
15 to

$$16 \quad \bar{N}_{INP}(k, t) = \iiint N_{INP}(x, y, z, k, t) \, dx \, dy \, dz. \quad (3)$$

17 Upon sublimation, the modification of activation thresholds that can occur for previously  
18 nucleated INP, i.e. preactivation (Roberts and Hallett, 1967), is not considered and  $N_{INP}$  are  
19 returned to each bin  $k$  with weighting

$$20 \quad W_k = [\bar{N}_{INP}(k, 0) - \bar{N}_{INP}(k, t)] / \bar{N}_{INP}(k, 0) \quad (4)$$

21 where  $W_k$  is normalized such that  $\sum W_k = 1$ . The  $W_k$  are recalculated each time step. In this  
22 way, INP are recycled preferentially to each of the eight temperature bins from which they  
23 originated (Feingold et al., 1996).

## 24 **4 Simulations Completed**



1 Simulations completed for this study are listed in Table 1. A simulation with INP and CCN  
2 factors equal to 1.0 is referred to as the Control. To isolate the impact of CCN perturbations  
3 on mixed-phase clouds without a change in ice formation, three simulations were run with  
4 CCN factors 1/2, 1, 2 and INP factors equal to 1.0 (runs ConIce0.5, Control, ConIce2.0). To  
5 identify the impact of CCN perturbations on mixed-phase clouds when ice formation is a linear  
6 function of the CCN number concentration, two runs were done with INP and CCN factors  
7 equal to 2, one with fixed CCN (FixedCCN2.0) and one with prognostic CCN (LinIce2.0), and  
8 one run with INP and CCN factors equal to 1/2 (LinIce0.5).

## 9 **5 Model Results**

### 10 ***a. Control simulation***

11 The control simulation (CCN and INP factors equal to one) has IWP and LWP consistent with  
12 observations on 17 April 2015 (Figures 1b and 3a), and a cloud system that reaches a steady  
13 state after 5 hours with liquid water fractions close to 0.5. The cloud-driven mixed-layer depth  
14 slowly increases over the 16-hour integration, with both cloud top rising and cloud base  
15 lowering at a rate of  $\sim 5$  m/hour. However, the cloud system remains decoupled from the  
16 surface layer and a surface inversion of  $\sim 180$  meters in depth is maintained throughout the  
17 integration.

18 Rain forms in the liquid layer (with concentrations less than  $0.02 \text{ cm}^{-3}$ ) and evaporates within  
19 200 meters of cloud base. Therefore, the production and impact of rain on this simulation can  
20 be neglected. This is true for the sensitivity studies discussed below as well but would not be  
21 the case for runs with more limited CCN, which would produce significant precipitation.

22 Snow does reach the surface during the steady state with a relatively constant flux of  $6 \times 10^{-4} \text{ g}$   
23  $\text{m}^{-2} \text{ s}^{-1}$ . Sublimation at the base of the cloud-driven mixed-layer reduces the snow water content  
24 by  $6 \times 10^{-6} \text{ g m}^{-3} \text{ s}^{-1}$ . In terms of number concentration, this causes the recycling of  
25 approximately  $1 \text{ L}^{-1} \text{ hour}^{-1}$  of INP back into the cloud-driven mixed-layer. Since total ice  
26 crystal number concentrations are  $1\text{--}2 \text{ L}^{-1}$  in the mixed-layer over the integration, this indicates  
27 that recycling of INP is playing a significant role in the maintenance of cloud ice in this cloud  
28 system (e.g., Solomon et al. 2015).



1 While the cloud system is maintaining a steady state in cloud ice and liquid, longwave cooling  
2 continually cools the cloud-driven mixed-layer, contributing to the maintenance of the phase-  
3 partitioning by increased activation of INP within the liquid cloud layer and depletion of water  
4 vapor within the mixed-layer. This cooling is required to maintain the cloud liquid because of  
5 the continuous depletion of water vapor, and to maintain the cloud ice, since  $\sim 2 \text{ L}^{-1}$  of INP are  
6 lost to the surface through precipitation each hour.

### 7 ***b. Impact of CCN perturbations with constant ice formation***

8 The first set of simulations completed for this study tests the sensitivity of the cloud to  
9 perturbations in CCN concentrations, while keeping INP concentrations fixed (ConIce  
10 simulations). Simulations involved increasing and decreasing the initial CCN concentrations  
11 by a factor of two. These runs provide insight into the impact of CCN perturbations in an Arctic  
12 environment with stable stratification near the surface and a weak inversion at cloud top with  
13 relatively moist air. Figure 3a shows that increasing the CCN concentrations has the expected  
14 effect at the beginning of the integrations when the cloud layer is optically thin-- smaller  
15 droplets increase the cloud emissivity and thereby longwave cooling at cloud top, increasing  
16 turbulence, supersaturation, and droplet formation. The opposite result is found with  
17 decreasing CCN concentrations. For these optically thin cases, radiative cooling is a  
18 contribution from the full physical depth of the cloud and the increased cooling rate is therefore  
19 an expression of increased total emission of the cloud. Figure 3b shows that this also results in  
20 faster vapor deposition rates, resulting in increased ice mass given an increase in CCN.  
21 However, this increase in IWP plateaus and slowly decreases after hours 5-6 as ice crystals fall  
22 out of the cloud layer and are lost from the system. Decreasing CCN results in slower  
23 deposition rates and reduced IWP.

24 What is unexpected is that the minimum longwave heating rate (or maximum cooling rate) is  
25 not exclusively a function of LWP, even after the clouds become optically thick (Figure 3c).  
26 The larger longwave cooling rate associated with a cloud forming in conjunction with elevated  
27 CCN concentrations causes increased total water in the cloud-driven mixed-layer (indicating  
28 that liquid water increases faster than ice mass), which increases the water vapor mixing ratio  
29 below the liquid layer, increasing relative humidity in the mixed-layer below the liquid layer



1 (see Figure 4a). The IWP shows larger temporal variability than the LWP, potentially due to  
2 larger sensitivity to small perturbations in relative humidity.

3 Increasing CCN causes the cloud top to rise and the cloud base to lower faster while keeping  
4 the maximum buoyancy relatively unchanged, the maximum buoyancy as a function of LWP  
5 is similar for ConIce2.0 and Control, with Control approximately  $1 \times 10^{-4}$  less than ConIce2.0  
6 for LWP less than  $17 \text{ gm}^{-2}$  (Figure 3d). The deepening of the cloud layer for an increase in  
7 CCN causes the impact of CCN on maximum droplet size to persist throughout the integration  
8 (Figure 5a), even though LWP is increasing more rapidly (Figure 3a).

9 The ConIce set of simulations was designed to identify the impact of CCN variability on phase-  
10 partitioning and cloud dynamics for a relatively constant magnitude of cloud ice number  
11 concentration. This is seen to be the case in Figure 5c, however, interestingly, processes such  
12 as sublimation cause ConIce2.0 to have less total cloud ice number concentration than the other  
13 two runs (see Figure 4a-d), since a reduction in sublimation causes more INP to fall out of the  
14 mixed-layer and less recycling of INP in the cloud layer. However, the differences in relative  
15 humidity also play a role here and therefore the sublimation rate is not just a function of the  
16 ice present. Increasing CCN causes more rapid mixed-layer cooling (Figure 4b and 5b) and  
17 deeper mixed-layer depths, and therefore larger net deposition rates (Figure 5d) and larger  
18 IWPs (Figure 3b).

### 19 ***c. Impact of CCN perturbations with linear ice formation***

20 A second set of simulations was completed adding an additional degree of realism to the  
21 simulations by scaling INP concentrations with the CCN concentration, i.e., equal INP and  
22 CCN factors (LinIce simulations). This was done in order to represent the case of a polluted  
23 air mass with equal relative increases of CCN and INP. The fraction of INP to CCN evolves  
24 in time as cloud ice forms and precipitates, sublimates below the cloud base, and advects back  
25 into the cloud layer with the cloud-driven vertical motions.

26 Figure 6 shows the sensitivity of the LWP and IWP to an increase and decrease in CCN and  
27 INP by a factor of 2. Similar to the ConIce runs, the increase in LWP begins to slow when IWP  
28 exceeds  $20 \text{ g m}^{-2}$ . Before hour 5 the ConIce and LinIce runs have similar trajectories. After



1 hour 5 these runs diverge; decreasing CCN and INP factors in LinIce results in larger LWP  
2 because of the dominating effect of INP variability on water vapor availability. Increasing  
3 CCN and INP factors from 0.5 to 1.0 results in a 63% decrease in LWP at hour 15.

4 The LinIce runs highlight the extreme sensitivity of phase-partitioning between cloud liquid  
5 and ice to very small changes in INP concentrations. For these simulations, there are 5 orders  
6 of magnitude difference between CCN and INP concentrations, with the scaling done on a  
7 percentage basis relative to the absolute amount. In other words, a change in INP from 1 to 2  
8  $L^{-1}$  has a substantially larger effect on cloud phase than a change in CCN from 10,000 to 20,000  
9  $L^{-1}$ , despite the latter change obviously being much more extreme from the perspective of  
10 aerosol number concentration. The CCN variability in the LinIce runs cause a 50% increase in  
11 droplet effective radius for a decrease in CCN by a factor of two (Figure 7a). These changes  
12 are of the same sign as the ConIce runs but are larger due to the additional impact of INP  
13 variability on water vapor available for condensation. Similarly, the reduction of cloud droplet  
14 size related to the presence of elevated aerosol concentrations is exacerbated when both INP  
15 and CCN concentrations increase due to the combination of more nucleated droplets (on CCN)  
16 and increased water vapor deposition (on ice crystals generated by the elevated INP  
17 concentrations). However, the impact of the changes in droplet effective radius are small  
18 relative to the impact of INP variability on the dynamics of the cloud-driven mixed layer after  
19 approximately hour 4. For example, after hour 7 the LinIce0.5 run has a colder cloud-driven  
20 mixed-layer than the Control and LinIce2.0 runs (Figure 7b), whereas ConIce2.0 had a colder  
21 cloud-driven mixed-layer than ConIce0.5 (Figure 5b).

22 The ratio of INP among the LinIce runs stays relatively constant for the 16-hour integrations  
23 (Figure 7c), indicating that differences in sublimation (INP recycling) and ice fall speeds do  
24 not produce appreciably different ice crystal number concentrations in the cloud-driven mixed-  
25 layer. However, larger deposition rates in the cloud-driven mixed-layer due to increased ice  
26 number concentrations (Figure 7d) result in larger ice water mixing ratios (a 31% increase  
27 between ConIce2.0 and LinIce2.0), even though mixed-layer temperatures are warmer for an  
28 increase in CCN and INP factors, indicating that NDEPS is dominant relative to ice number in  
29 controlling IWP.



1 Allowing both prognostic CCN and INP reveals interesting layering of aerosol distributions  
2 that results from differential liquid and ice processes. This is seen in Figure 8, where the  
3 turbulent advection of droplets into the cloud top inversion causes larger CCN concentrations  
4 above the liquid cloud layer than below (Figure 8a). The opposite result is found for INP, where  
5 gravitational settling of ice crystals and the subsequent sub-cloud sublimation produces  
6 locally-elevated INP concentrations in the lowest 200 meters (Figure 8b). This layering of  
7 aerosols causes larger entrainment of CCN at cloud top and larger entrainment of INP at mixed-  
8 layer base as the mixed-layer deepens. As was demonstrated in Solomon et al (2015), the  
9 increase in INP at the base of the mixed-layer contributed to the maintenance of the phase-  
10 partitioning by making more INP available for activation as ice crystals as the mixed-layer  
11 deepens.

12 This layering of aerosols, with increased CCN above the liquid layer and increased INP below  
13 the cloud-driven mixed-layer, causes interesting differences between runs with and without  
14 prognostic CCN (Figure 9). The increase in CCN above the liquid layer causes increased  
15 entrainment of CCN at cloud top (Figure 9a), decreasing the droplet effective radius, increasing  
16 the longwave cooling (Figure 9b), increasing the deposition rate and ice water mixing ratio  
17 (Figure 9c). Ultimately, these differences result in stronger buoyancy with the cloud layer  
18 (Figure 9d), where buoyancy is increased by up to 10%.

## 19 **6 Summary and Discussion**

20 In this study we use idealized large-eddy simulations to quantify the relative impact of CCN  
21 and INP perturbations on the phase-partitioning and dynamics of AMPS. The modeling  
22 framework developed in Solomon et al. (2015) to study the recycling of INP has been extended  
23 to include prognostic CCN. The first set of simulations were designed to investigate the impact  
24 of relatively small perturbations in CCN compared to studies such as Morrison et al. (2008)  
25 and Kravitz et al. (2014) in mixed-phase conditions with essentially constant INP on phase-  
26 partitioning and cloud dynamics. It is found that increasing CCN by a factor of two increases  
27 LWP by 60-100%, while decreases CCN by a factor of reduces LWP by less than 8%, i.e., the  
28 impact is highly non-linear. This change stems primarily from an increase in cloud longwave  
29 emissivity and associated increase of cloud-top cooling rates, connected to a decrease in



1 droplet size. This elevated cooling rate causes the cloud-driven mixed-layer to cool and deepen  
2 more rapidly. However, interestingly, this difference persists even when the cloud radiates as  
3 a blackbody, highlighting the influence of early changes to the system.

4 The sensitivity to CCN in this study is significantly larger than that found in the M-PACE case  
5 study by Morrison et al. (2008) and the ISDAC case study by Kravitz et al. (2014). The M-  
6 PACE and ISDAC case studies are useful as examples of the extreme range of conditions under  
7 which mixed-phase clouds exist. M-PACE took place in October over open water with large  
8 fluxes of heat and momentum from the surface into the cloud layer, while ISDAC took place  
9 during the spring when the Arctic Ocean was essentially ice-covered and the cloud layer was  
10 decoupled from the surface layer.

11 In the M-PACE case study increasing CCN by a factor of 5-6 resulted in an increase in LWP  
12 by 20% and a decrease in IWP by 60%. In the ISDAC case study, increasing CCN by a factor  
13 of 4 resulted in similar LWP and IWP until hour 12 when the more pristine cloud collapsed. A  
14 very interesting difference between this study and the two previous studies is that both the M-  
15 PACE and ISDAC studies found IWP to decrease when CCN was increased, while this study  
16 finds an increase in IWP due to increased longwave cooling and larger deposition rates. For  
17 the ISDAC case study this may be due to the continuous decrease in droplet number  
18 concentration, which would cause the cloud dynamics to spin down. This study also finds a  
19 significantly larger sensitivity to INP than the M-PACE case study. The M-PACE case study  
20 found that a 10X increase in INP resulted in a 120% increase in IWP and a 23% decrease in  
21 LWP, while this study finds increasing INP by 2X results in a 60% increase in IWP and a 36%  
22 decrease in LWP. These differences need to be investigated further to identify the relative  
23 impact of different environmental conditions and model physics.

24 The differences between this study and the M-PACE and ISDAC studies are due in part to the  
25 different environmental conditions but the different sensitivities to both CCN and INP are also  
26 due to the different parameterizations used in these models. Both the M-PACE and ISDAC  
27 studies essentially hold INP fixed, while this study does not constrain INP other than specifying  
28 an initial value. This allows for the vertical redistribution of particles throughout the domain,



1 resulting in feedbacks between ice and droplet properties and cloud dynamics not included in  
2 the two previous case studies and in many climate and weather-scale models.

3 Additionally, the inclusion of prognostic CCN and INP reveals a number of feedbacks that  
4 buffer the cloud system from collapsing. The first buffering feedback is the recycling of INP,  
5 which was the focus of the Solomon et al. (2015) study. The IWP, and therefore phase-  
6 partitioning between cloud ice and liquid, cannot be maintained without this feedback.  
7 However, the reservoir of INP below the mixed-layer would be depleted if cloud-driven mixed-  
8 layer became coupled to the surface layer. The second interesting buffering feedback is the  
9 layering of the aerosols, with increased concentrations of CCN above cloud top and increased  
10 concentrations of INP at the base of the mixed-layer. As demonstrated in this paper, this  
11 layering contributes to the maintenance of the cloud liquid, which ultimately drives the  
12 dynamics of the cloud system. A third buffering feedback is the thinning of the liquid layer  
13 when INP concentrations are increased. The occurrence of this thinning does not produce  
14 complete glaciation, rather causes the mixed-phase clouds to radiate as grey bodies and the  
15 radiative properties of the clouds to be more sensitive to aerosol perturbations.

16 Ultimately, enhanced observations of the vertical structure of cloud microphysics and aerosol  
17 properties are required. Recent work by the DOE ARM program to operate unmanned aircraft  
18 and tethered balloons has provided new perspectives on these quantities and the dynamic and  
19 thermodynamic conditions supporting these cloud systems (de Boer et al. 2018). Such  
20 observational efforts should continue to be pursued further to help constrain the sensitivities  
21 demonstrated by numerical studies as presented here.

## 22 **7 Acknowledgments**

23 This research was supported by the US Department of Energy (DOE) Atmospheric Systems  
24 Research (ASR) program (DE-SC0013306) and the National Oceanic and Atmospheric  
25 Administration (NOAA) Physical Sciences Division (PSD). Additionally, measurements used  
26 in this study were supported by the US Department of Energy Atmospheric Radiation  
27 Measurement (ARM) program.



1 **8 References**

- 2 Abdul-Razzak, H., and Ghan, S. J.: A parameterization of aerosol activation 2. Multiple aerosol  
3 types, *J. Geophys. Res.*, **105**, 6837–6844, 2000.
- 4 Albrecht, B. A.: Aerosols, cloud microphysics, and fractional cloudiness, *Science*, **245**, 1227–  
5 1230, 1989.
- 6 Bergeron, T.: in *Proces Verbaux de l'Association de Meteorologie* (ed. Duport, P.) 156-178  
7 (International Union of Geodesy and Geophysics, 1935).
- 8 Cziczo, D., Froyd, K., Gallavardin, S., Moehler, O., Benz, S., Saathoff, H., and Murphy, D.:  
9 Deactivation of ice nuclei due to atmospherically relevant surface coatings, *Environ.*  
10 *Res. Lett.*, **4**:044013, doi:10.1088/1748-9326/4/4/044013, 2009.
- 11 Curry, J. A., and Ebert, E. E.: Annual cycle of radiation fluxes over the Arctic Ocean:  
12 Sensitivity to cloud optical properties. *J. Climate.*, **5**, 1267-1280, 1992.
- 13 Curry, J. A., Schramm, J. L., and Ebert, E. E.: Impact of clouds on the surface radiation balance  
14 of the ocean, *Meteor. Atmos. Phys.*, **51**, 197-217, 1993.
- 15 de Boer, G., and co-authors: A bird's-eye view: Development of an operational ARM  
16 unmanned aerial capability for atmospheric research in Arctic Alaska, *Bull. Amer.*  
17 *Meteor. Soc.*, early online release, 2018.
- 18 de Boer, G., Morrison, H., Hildner, R., and Shupe, M. D.: Evidence of liquid-dependent ice  
19 nucleation in high-latitude stratiform clouds from surface remote sensors, *Geophys.*  
20 *Res. Lett.*, **38**, L01803, 2011.
- 21 DeMott, P. J.: An exploratory study of ice nucleation by soot aerosols, *J. Appl. Meteorol.*,  
22 **29**(10), 1072–1079, 1990.
- 23 DeMott, P. J., Prenni, A. J., Liu, X., Petters, M. D., Twohy, C. H., Richardson, M. S.,  
24 Eidhammer, T., Kreidenweis, S. M., and Rogers, D. C.: Predicting global atmospheric ice  
25 nuclei distributions and their impacts on climate, *P. Natl. Acad. Sci.*, **107**, 11217-11222,  
26 doi:10.1073/pnas.0910818107, 2010.
- 27 DeMott, P. J., Prenni, A. J., McMeeking, G. R., Sullivan, R. C., Petters, M. D., Tobo, Y.,  
28 Niemand, M., Möhler, O., Snider, J. R., Wang, Z., and Kreidenweis, S. M.: Integrating  
29 laboratory and field data to quantify the immersion freezing ice nucleation activity of  
30 mineral dust particles, *Atmos. Chem. Phys.*, **15**, 393-409, doi:10.5194/acp-15-393-  
31 2015, 2015.



- 1 Dyer, A. J., and Hicks, B. B.: Flux-gradient relationships in the constant flux layer, *Q. J. Roy.*  
2 *Meteor. Soc.*, **96**, 715–721, 1970.
- 3 Earle, M. E., Liu, P. S., Strapp, J. W., Zelenyuk, A., Imre, D., McFarquhar, G. M., Shantz, N.  
4 C., and Leaitch, W. R.: Factors influencing the microphysics and radiative properties of  
5 liquid-dominated Arctic clouds: Insight from observations of aerosol and clouds during  
6 ISDAC, *J. Geophys. Res. – Atmos.*, **116**, D00T09, [10.1029/2011jd015887](https://doi.org/10.1029/2011jd015887), 2011.
- 7 Feingold, G., Kreidenweis, S. M., Stevens, B., and Cotton, W. R.: Numerical simulation of  
8 stratocumulus processing of cloud condensation nuclei through collision-coalescence, *J.*  
9 *Geophys. Res.*, **101**, 21,391-21,402, 1996.
- 10 Findeisen, W.: *Kolloid-Meteorologische* 2nd edn (American Meteorological Society, 1938).
- 11 Garimella, S., Rothenberg, D. A., Wolf, M. J., David, R. O., Kanji, Z. A., Wang, C., Roesch,  
12 M., and Cziczo, D. J.: Uncertainty in counting ice nucleating particles with continuous  
13 diffusion flow chambers, *Atmos. Chem. Phys.*, doi:10.5194/acp-2016-1180, 2017.
- 14 Garrett, T., and Zhao, C.: Increased Arctic cloud longwave emissivity associated with  
15 pollution from mid-latitudes. *Nature*, **440**, 787–789, 2006.
- 16 Garrett, T. J., Radke, L. F., and Hobbs, P. V.: Aerosol effects on cloud emissivity and surface  
17 longwave heating in the Arctic, *J. Atmos. Sci.*, **59**, 769-778, 2002.
- 18 Girard, E., and Sokhandan, A. N.: Relative importance of acid coating on ice nuclei in the  
19 deposition and contact modes for wintertime Arctic clouds and radiation. *Meteorol. Atmos.*  
20 *Phys.*, **123**(1):81-92, 2014.
- 21 Hobbs, P., and Rangno, A.: Microstructures of low and middle-level clouds over the Beaufort  
22 Sea. *Q. J. Roy. Meteor. Soc.* **124**, 2035–2071, 1998.
- 23 Intrieri, J. M., Shupe, M. D., Uttal, T., and McCarty, B. J.: An annual cycle of Arctic cloud  
24 characteristics observed by radar and lidar at SHEBA, *J. Geophys. Res.*, **107**, 8030,  
25 doi:10.1029/2000JC000423, 2002.
- 26 Lance, S., Shupe, M. D., Feingold, G., Brock, C. A., Cozic, J., Holloway, J. S., Moore, R. H.,  
27 Nenes, A., Schwarz, J. P., Spackman, J. R., Froyd, K. D., Murphy, D. M., Brioude, J.,  
28 Cooper, O. R., Stohl, A., and Burkhardt, J. F.: Cloud condensation nuclei as a modulator of  
29 ice processes in Arctic mixed-phase clouds, *Atmos. Chem. Phys.*, **11**, 8003-8015,  
30 <https://doi.org/10.5194/acp-11-8003-2011>, 2011.



- 1 McFarquhar, G. M., Zhang, G., Poellot, M. R., Kok, G. L., McCoy, R., Tooman, T., and  
2 Heymsfield, A. J.: Ice properties of single layer stratocumulus during the Mixed-Phase  
3 Arctic Cloud Experiment (MPACE). Part I: Observations, *J. Geophys. Res.*, **112**, D24202,  
4 doi:10.1029/2007JD008646, 2007.
- 5 McFarquhar, G., and coauthors.: Indirect and semi-direct aerosol campaign: The impact of  
6 Arctic aerosols on clouds, *Bull. Am. Meteorol. Soc.* **92**, 183–201, 2011.
- 7 Mlawer, E. J., Taubman, S. J., Brown, P. D., Iacono, M. J., and Clough, S. A.: Radiative  
8 transfer for inhomogeneous atmospheres: RRTM, a validated correlated- $k$  model for  
9 the longwave, *J. Geophys. Res.*, **102**, 16663–16682, 1997.
- 10 Morrison, H., and Pinto, J. O.: Mesoscale modeling of springtime Arctic mixed-phase  
11 stratiform clouds using a new two-moment bulk microphysics scheme, *J. Atmos. Sci.*, **62**,  
12 3683-3704, 2005.
- 13 Morrison, H., Thompson, G., and Tatarskii, V.: Impact of cloud microphysics on the  
14 development of trailing stratiform precipitation in a simulated squall line: Comparison of  
15 one- and two-moment schemes, *Mon. Wea. Rev.*, **137**, 991-1007,  
16 doi:10.1175/2008MWR2556.1, 2009.
- 17 Morrison, H., Pinto, J. O., Curry, J. A., and McFarquhar, G. M.: Sensitivity of modeled arctic  
18 mixed-phase stratocumulus to cloud condensation and ice nuclei over regionally varying  
19 surface conditions, *J. Geophys. Res.*, **113**, D05203, doi:10.1029/2007JD008729, 2008.
- 20 Murray, B. J., O’Sullivan, D., Atkinson, J. D., and Webb, M. E.: Ice nucleation by particles  
21 immersed in supercooled cloud droplets, *Chem. Soc. Rev.* **41**, 6519–6554, 2012.
- 22 Paulson, C. A.: The mathematical representation of wind speed and temperature profiles in the  
23 unstable atmospheric surface layer, *J. Appl. Meteor.*, **9**, 857–861, 1970.
- 24 Pincus, R., and Baker, M.B.: Effect of precipitation on the albedo susceptibility of marine  
25 boundary layer clouds, *Nature*, **372**, 250–252, 1994.
- 26 Pruppacher, H. R., and Klett, J. D.: *Microphysics of Clouds and Precipitation*, 2nd ed., Kluwer,  
27 Dordrecht, Netherlands, 1997.
- 28 Shupe, M. D., and Intrieri, J. M.: Cloud radiative forcing of the Arctic surface: The influence  
29 of cloud properties, surface albedo, and solar zenith angle, *J. Climate*, **17**, 616-628, 2004.



- 1 Solomon, A., Feingold, G., and Shupe, M. D.: The role of ice nuclei recycling in the  
2 maintenance of cloud ice in Arctic mixed-phase stratocumulus, *Atmos. Chem. Phys.*, **15**,  
3 10631-10643, doi:10.5194/acp-15-10631-2015, 2015.
- 4 Stevens, B., and Feingold, G.: Untangling aerosol effects on clouds and precipitation in a  
5 buffered system, *Nature*, **461**, 607–613, 2009.
- 6 Stevens, B., Cotton, W., Feingold, G., and Moeng, C.: Large-eddy simulations of strongly  
7 precipitating, shallow, stratocumulus-topped boundary layers, *Journal of the Atmospheric*  
8 *Sciences*, **55**, 3616-3638, 1998.
- 9 Sullivan, R. C., Miambres, L., DeMott, P. J., Prenni, A. J., Carrico, C. M., Levin, E. J. T.,  
10 and Kreidenweis, S. M.: Chemical processing does not always impair heterogeneous ice  
11 nucleation of mineral dust particles, *Geophys. Res. Lett.*, **37**, L24805,  
12 doi:10.1029/2010GL045540, 2010.
- 13 Tewari, M., Chen, F., Wang, W., Dudhia, J., LeMone, M. A., Mitchell, K., Ek, M., Gayno,  
14 G., Wegiel, J., and Cuenca, R. H.: Implementation and verification of the unified  
15 NOAA land surface model in the WRF model. *20th conference on weather analysis*  
16 *and forecasting/16th conference on numerical weather prediction*, pp. 11–15, 2004.
- 17 Twomey, S.: Influence of pollution on shortwave albedo of clouds, *J. Atmos. Sci.* **34**, 1149–  
18 1152, 1977.
- 19 Webb, E. K.: Profile relationships: The log-linear range, and extension to strong stability,  
20 *Quart. J. Roy. Meteor. Soc.*, **96**, 67–90, 1970.
- 21 Wegener, A.: *Thermodynamik der Atmosphäre* (Leipzig, 1911).
- 22 Yamaguchi, T., and Feingold, G.: Technical note: Large-eddy simulation of cloudy boundary  
23 layer with the Advanced Research WRF model, *J. Adv. Model. Earth Syst.*, **4**, M09003,  
24 doi:10.1029/2012MS000164, 2012.
- 25 Zhang, T., Stamnes, K., and Bowling, S. A.: Impact of clouds on surface radiative fluxes and  
26 snowmelt in the Arctic and Subarctic, *J. Climate.*, **9**, 2110-2123, 1996.



1 **9 Tables**

Simulation Name	CCN Factor	INP Factor
<b>--Constant Ice Runs--</b>		
ConIce0.5 (red)	1/2	1
Control (black)	1	1
ConIce2.0 (blue)	2	1
<b>--Linear Ice Runs--</b>		
LinIce0.5 (red)	1/2	1/2
LinIce2.0 (blue)	2	2
FixCCN2.0	2	2

2 **Table 1:** Description of simulations completed and discussed in the paper.



## 1 10 Figure Captions

2 **Figure 1:** Measurements at Oliktok Point, Alaska 15-17 April 2015. (a) Ceilometer (black  
3 dots) and Ka-band cloud radar reflectivity (colored shading). B) LWP and IWP, in units of  $\text{gm}^{-2}$ .  
4  $^2$ . LW (c) and SW (d) surface radiation measurements, in units of  $\text{Wm}^{-2}$ . (e) Surface air  
5 temperatures. (f) Surface wind direction, in units of degrees. (g) Surface wind speed, in units  
6 of  $\text{ms}^{-1}$ . (h) Radiosondes at approximately 2330 UTC on 15 April, 1730 UTC and 2330 UTC  
7 on 16 April, and 1830 UTC and 2330 UTC on 17 April.

8 **Figure 2:** Sounding measured at 0 UTC 17 April 2015 at Oliktok Point, Alaska. Left: water  
9 vapor mixing ratio ( $q_v$ ) and potential temperature ( $\theta$ ), in units of  $\text{g kg}^{-1}$ , and Kelvin  
10 respectively. Right: zonal wind (U) and meridional wind (V), in units of  $\text{m s}^{-1}$ . The dashed  
11 lines show the initial profiles used in the WRFLES experiments. The dashed line overlying  
12 water vapor mixing ratio is the initial profile for the total water mixing ratio.

13 **Figure 3:** Time series from runs varying CCN concentrations with “constant” ice formation.  
14 a) LWP, in units of  $\text{gm}^{-2}$ . b) IWP, in units of  $\text{gm}^{-2}$ . c) Scatterplot of minimum longwave heating  
15 rate vs LWP, in units of  $\text{K hour}^{-1}$  and  $\text{g m}^{-2}$ , respectively. d) Scatterplot of integrated buoyancy  
16 vs LWP, in units of  $\text{m}^3\text{s}^{-3}$  and  $\text{g m}^{-2}$ , respectively. For INP factors equal to 1.0 and CCN factors  
17 2.0 (blue), 1.0 (black), and 0.5 (red).

18 **Figure 4:** Impact of increasing CCN by 2X (ConIce2.0 minus ConIce1.0) on (a) relative  
19 humidity, (b) sublimation rate, (c) water vapor mixing ratio, and (d) temperature, in units of  
20 percent,  $\text{g m}^{-3} \text{s}^{-1}$ ,  $\text{g kg}^{-1}$ ,  $^{\circ}\text{C}$ , respectively.

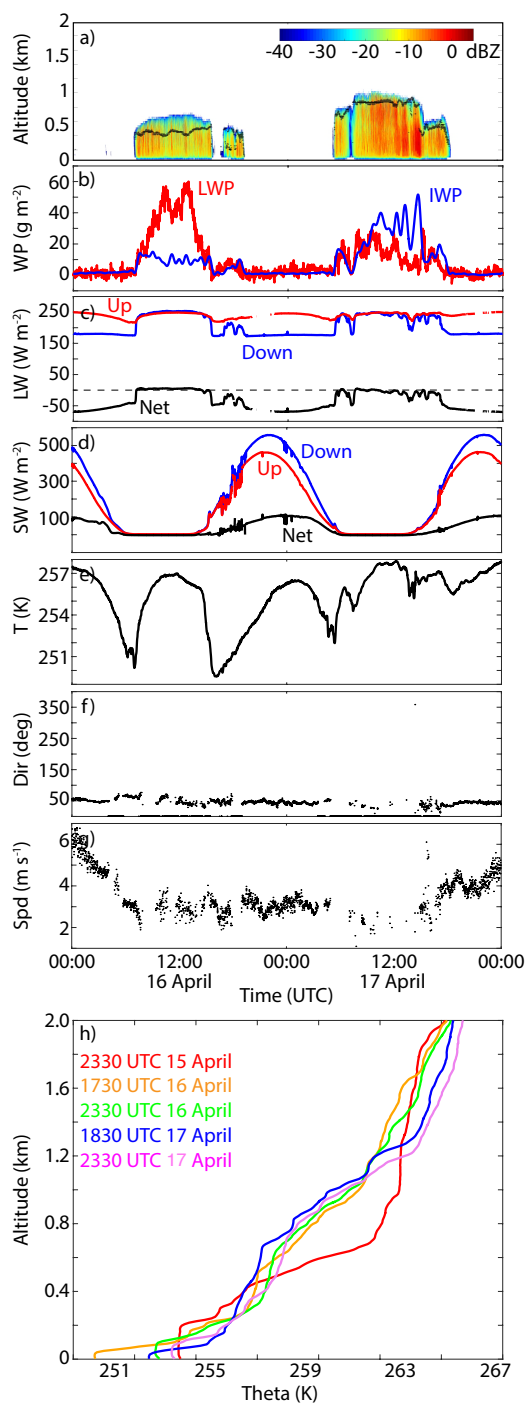
21 **Figure 5:** Time series from runs varying CCN concentrations with “constant” ice formation.  
22 a) Maximum effective radius, in units of microns. b) Cloud mixed-layer liquid-ice water static  
23 energy, in units Kelvin. c) Cloud base ice plus snow number concentration, in units of  $\text{L}^{-1}$ . d)  
24 Vertically integrated net deposition rate, in units of  $\text{g m}^{-2} \text{day}^{-1}$ . For CCN factors 0.5 (red), 1.0  
25 (black), and 2.0 (blue). For INP factors equal to 1.0 and CCN factors 0.5 (red), 1.0 (black), and  
26 2.0 (blue).



- 1 **Figure 6:** Time series from runs varying CCN concentrations with “linear” ice formation. a)  
2 LWP, in units of  $\text{gm}^{-2}$ . b) IWP, in units of  $\text{gm}^{-2}$ . c) Liquid water fraction for ConIce (solid) and  
3 LinIce (dashed). For CCN and INP factors 0.5 (red), 1.0 (black), and 2.0 (blue).
- 4 **Figure 7:** Time series from runs varying CCN concentrations with “linear” ice formation. a)  
5 Maximum effective radius, in units of microns. b) Cloud mixed-layer liquid-ice water static  
6 energy, in units Kelvin. c) Cloud base ice plus snow number concentration, in units of  $\text{L}^{-1}$ . d)  
7 Vertically integrated net deposition rate, in units of  $\text{g m}^{-2} \text{day}^{-1}$ . For CCN and INP factors 0.5  
8 (red), 1.0 (black), and 2.0 (blue).
- 9 **Figure 8:** (a) CCN and (b) INP in “linear” ice runs at hour 10, in units of  $\text{cm}^{-3}$  and  $\text{L}^{-1}$ ,  
10 respectively. For CCN and INP factors 0.5 (red), 1.0 (black), and 2.0 (blue).
- 11 **Figure 9:** Impact of prognostic CCN (LinIce2.0-FixCCN2.0) over hour 10. a) Droplet number  
12 concentration (black) and snow mixing ratio (red), in units of  $\text{cm}^{-3}$  and  $1.\text{e}^4 \cdot \text{g kg}^{-1}$ ,  
13 respectively. b) Longwave radiative heating rate, in units of  $\text{K hour}^{-1}$ . c) Liquid water content,  
14 in units of  $\text{g m}^{-3}$ . d) Buoyancy, in units of  $\text{m}^2 \text{s}^{-3}$ .



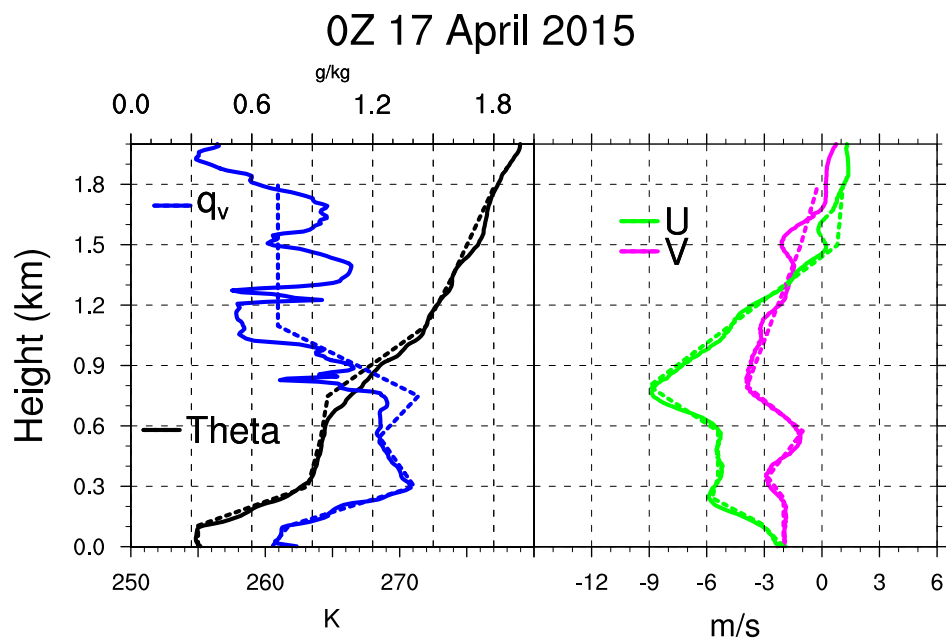
1



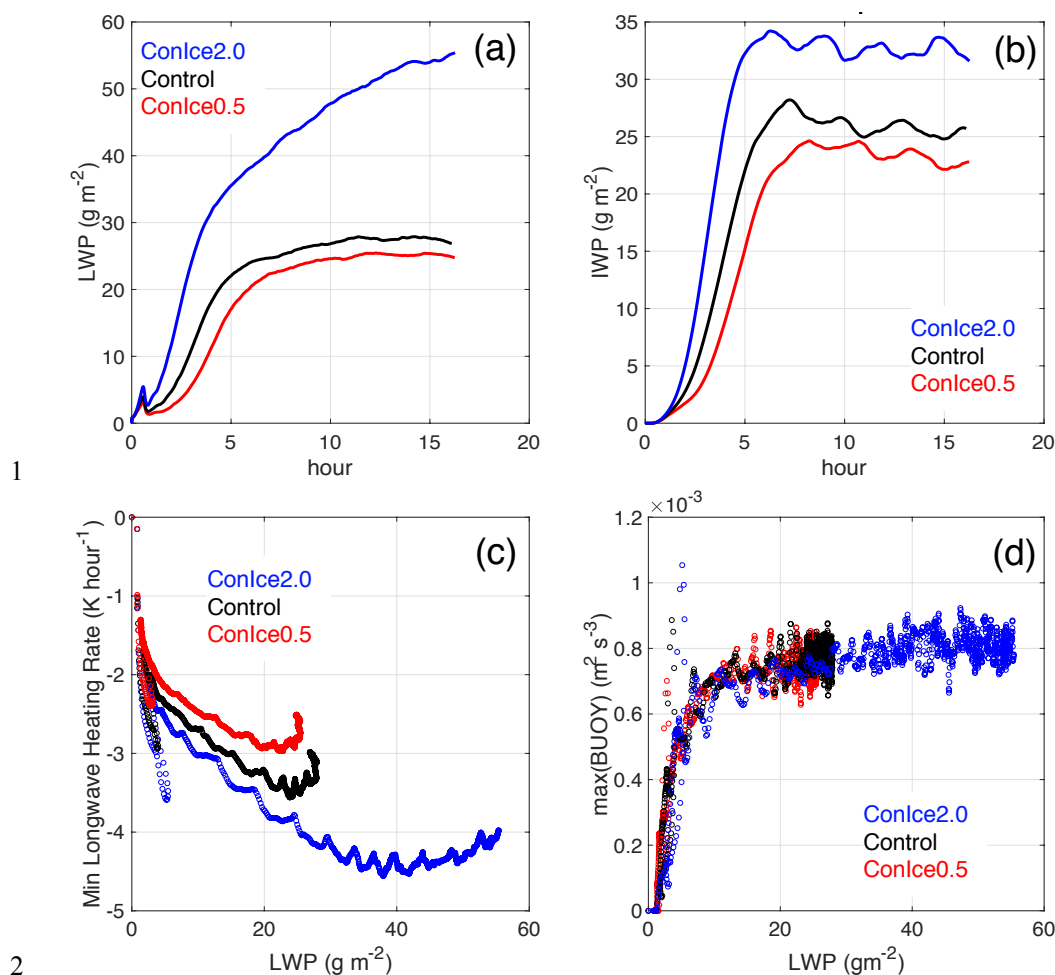
2



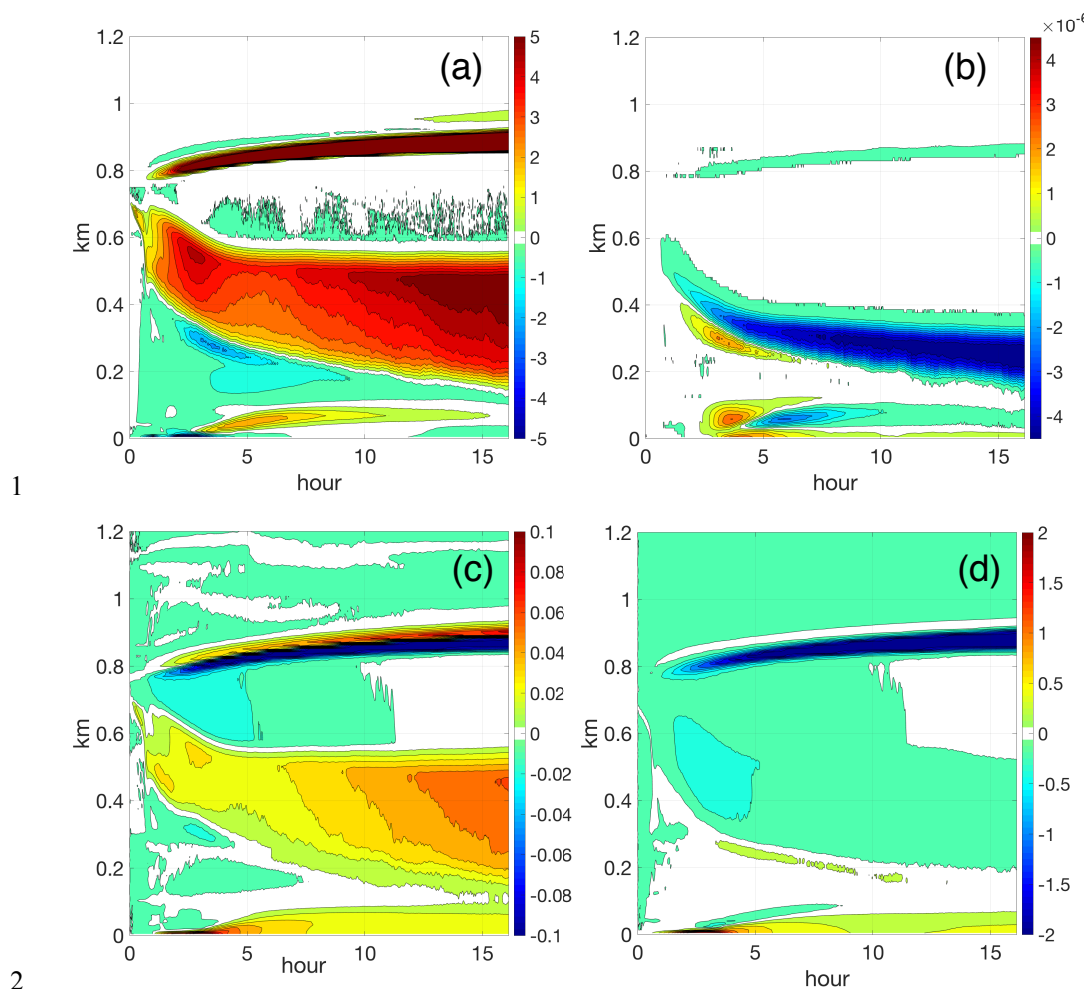
1 **Figure 1:** Measurements at Oliktok Point, Alaska 15-17 April 2015. (a) Ceilometer (black  
2 dots) and Ka-band cloud radar reflectivity (colored shading). B) LWP and IWP, in units of  
3  $\text{gm}^{-2}$ . LW (c) and SW (d) surface radiation measurements, in units of  $\text{Wm}^{-2}$ . (e) Surface air  
4 temperatures. (f) Surface wind direction, in units of degrees. (g) Surface wind speed, in units  
5 of  $\text{ms}^{-1}$ . (h) Radiosondes at approximately 2330 UTC on 15 April, 1730 UTC and 2330 UTC  
6 on 16 April, and 1830 UTC and 2330 UTC on 17 April.



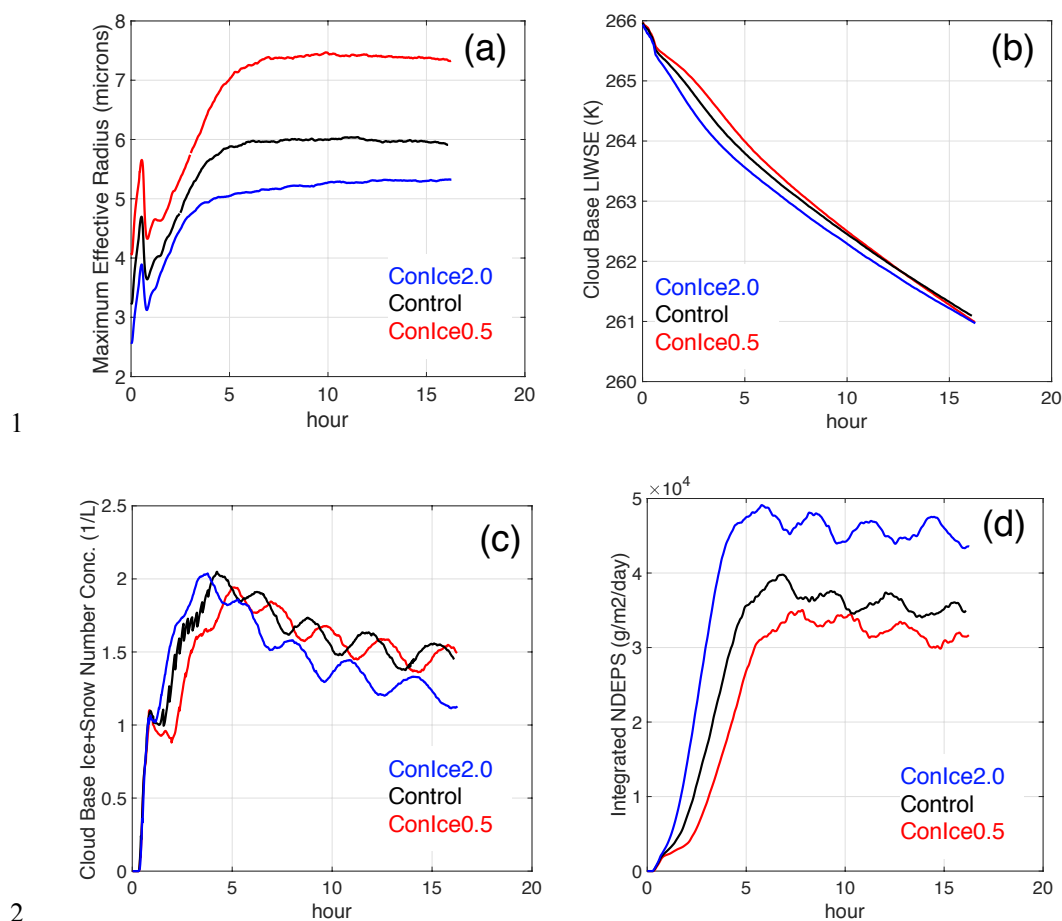
1  
2 **Figure 2:** Sounding measured at 0 UTC 17 April 2015 at Oliktok Point, Alaska. Left: water  
3 vapor mixing ratio ( $q_v$ ) and potential temperature (theta), in units of  $g\ kg^{-1}$ , and Kelvin  
4 respectively. Right: zonal wind (U) and meridional wind (V), in units of  $m\ s^{-1}$ . The dashed  
5 lines show the initial profiles used in the WRFLES experiments. The dashed line overlying  
6 water vapor mixing ratio is the initial profile for the total water mixing ratio.



1  
2  
3 **Figure 3:** Time series from runs varying CCN concentrations with “constant” ice formation.  
4 a) LWP, in units of  $\text{g m}^{-2}$ . b) IWP, in units of  $\text{g m}^{-2}$ . c) Scatterplot of minimum longwave heating  
5 rate vs LWP, in units of  $\text{K hour}^{-1}$  and  $\text{g m}^{-2}$ , respectively. d) Scatterplot of integrated buoyancy  
6 vs LWP, in units of  $\text{m}^3 \text{s}^{-3}$  and  $\text{g m}^{-2}$ , respectively. For CCN factors 2.0 (blue), 1.0 (black), and  
7 0.5 (red).



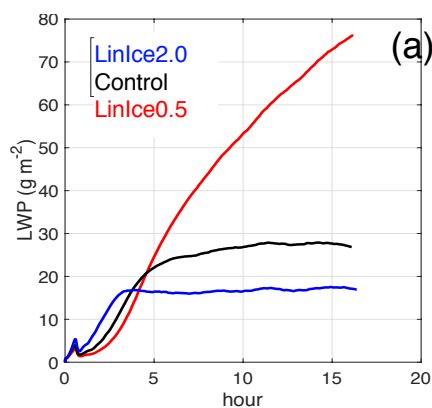
2  
3 **Figure 4:** Impact of increasing CCN by 2X (ConIce2.0 minus ConIce1.0) on (a) relative  
4 humidity, (b) sublimation rate, (c) water vapor mixing ratio, and (d) temperature, in units of  
5 percent,  $\text{g m}^{-3} \text{s}^{-1}$ ,  $\text{g kg}^{-1}$ ,  $^{\circ}\text{C}$ , respectively.



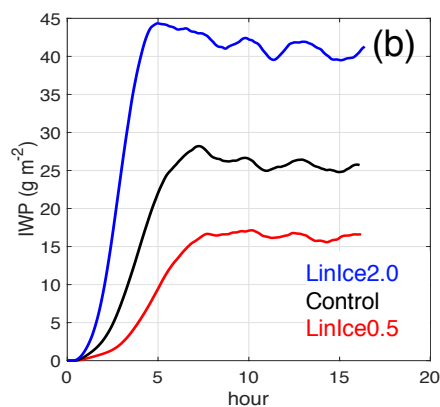
3 **Figure 5:** Time series from runs varying CCN concentrations with “constant” ice formation.  
4 a) Maximum effective radius, in units of microns. b) Cloud mixed-layer liquid-ice water static  
5 energy, in units Kelvin. c) Cloud base ice plus snow number concentration, in units of  $L^{-1}$ . d)  
6 Vertically integrated net deposition rate, in units of  $g\ m^{-2}\ day^{-1}$ . For CCN factors 0.5 (red), 1.0  
7 (black), and 2.0 (blue).



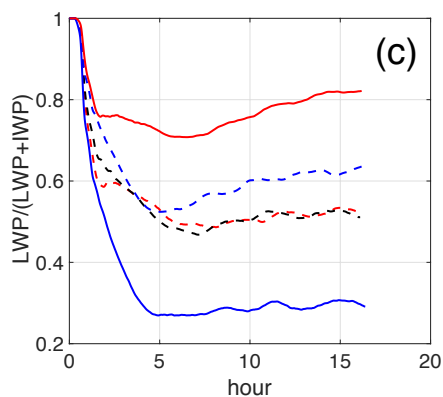
1



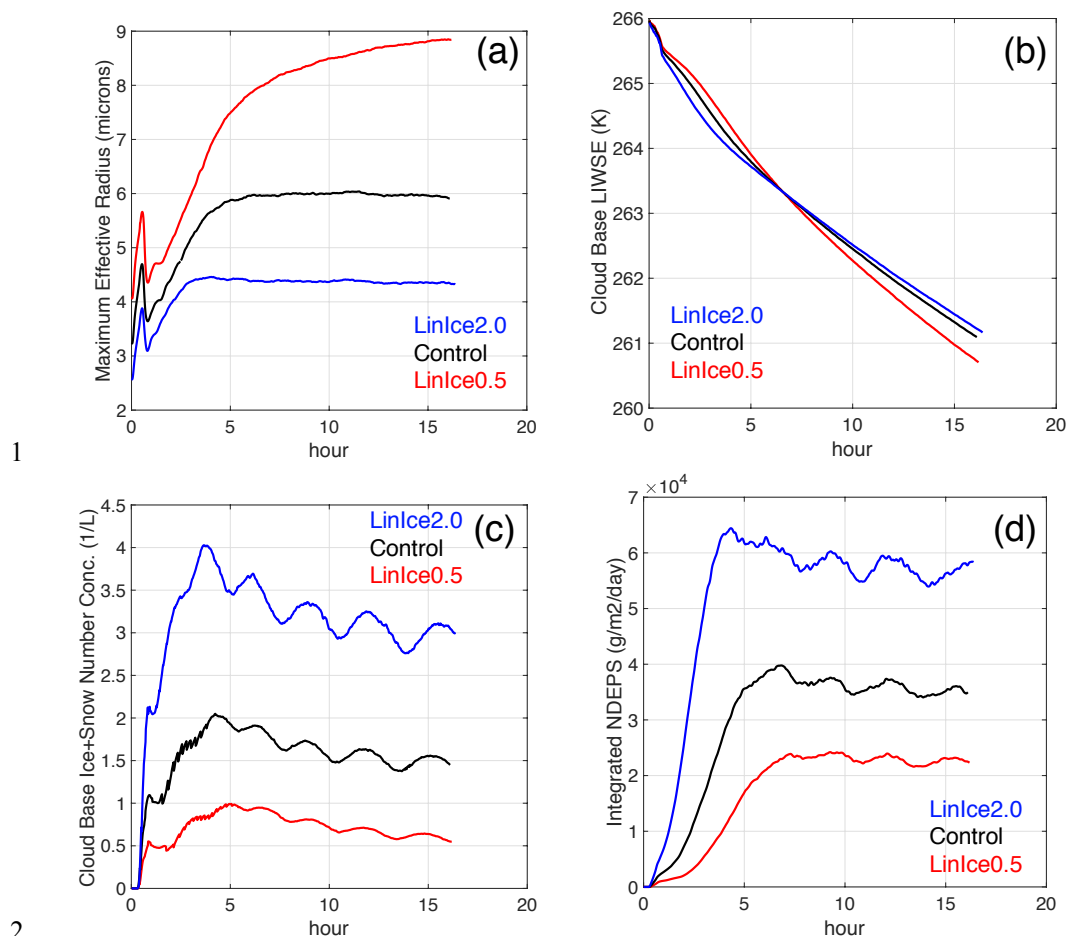
2



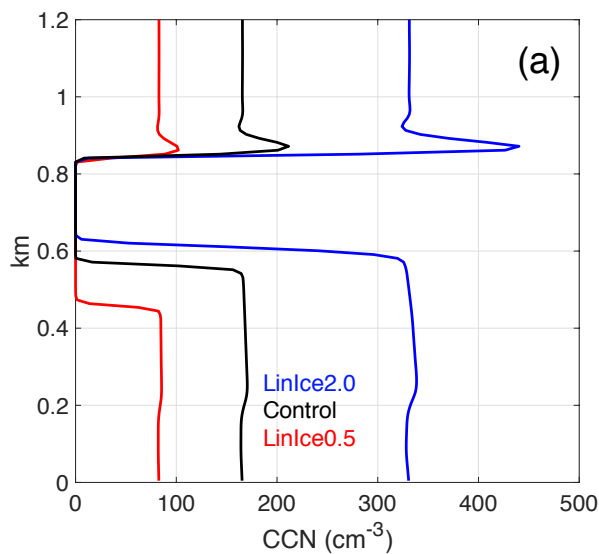
3



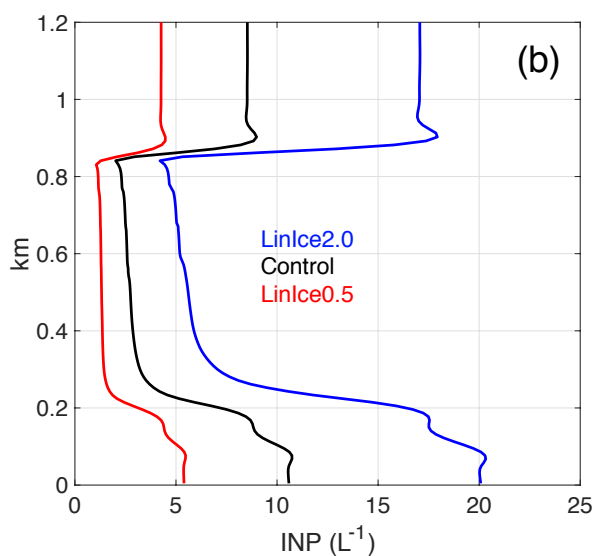
4 **Figure 6:** Time series from runs varying CCN concentrations with “linear” ice formation. a)  
5 LWP, in units of  $\text{g m}^{-2}$ . b) IWP, in units of  $\text{g m}^{-2}$ . c) Liquid water fraction for ConIce (dashed)  
6 and LinIce (solid). For CCN and INP factors 0.5 (red), 1.0 (black), and 2.0 (blue).



3 **Figure 7:** Time series from runs varying CCN concentrations with “linear” ice formation. a)  
4 Maximum effective radius, in units of microns. b) Cloud mixed-layer liquid-ice water static  
5 energy, in units Kelvin. c) Cloud base ice plus snow number concentration, in units of  $L^{-1}$ . d)  
6 Vertically integrated net deposition rate, in units of  $g\ m^{-2}\ day^{-1}$ . For CCN and INP factors 0.5  
7 (red), 1.0 (black), and 2.0 (blue).

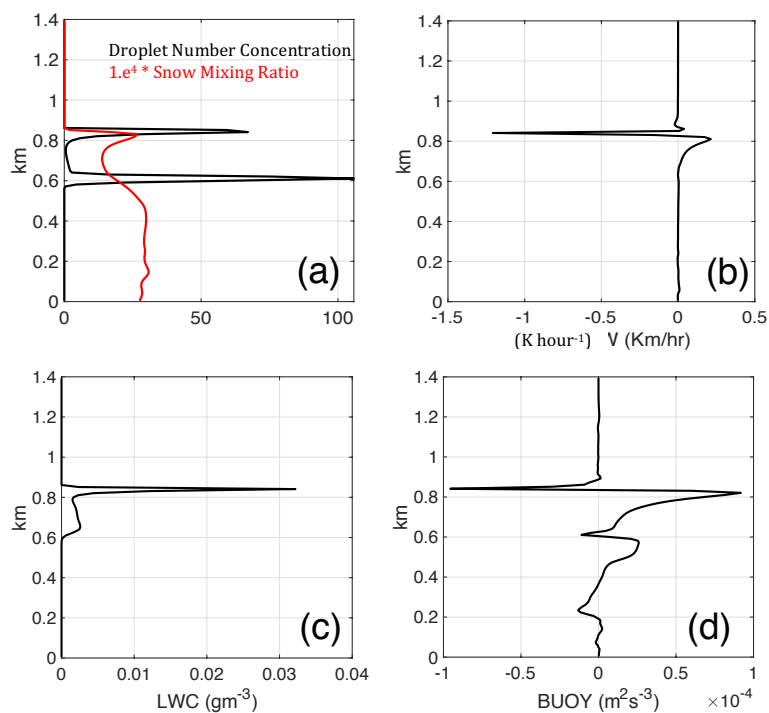


1



2

3 **Figure 8:** (a) CCN and (b) INP in “linear” ice runs at hour 10, in units of  $\text{cm}^{-3}$  and  $\text{L}^{-1}$ ,  
4 respectively. For CCN and INP factors 0.5 (red), 1.0 (black), and 2.0 (blue).



1

2

3

4 **Figure 9:** Impact of prognostic CCN (LinIce2.0-FixCCN2.0) over hour 10. a) Droplet  
5 number concentration (black) and snow mixing ratio (red), in units of cm<sup>-3</sup> and 1.e<sup>4</sup>\*g kg<sup>-1</sup>,  
6 respectively. b) Longwave radiative heating rate, in units of K hour<sup>-1</sup>. c) Liquid water  
7 content, in units of g m<sup>-3</sup>. d) Buoyancy, in units of m<sup>2</sup> s<sup>-3</sup>.